A Very High-Order Finite Volume Method Based on Weighted Least Squares for the Solution of Poisson Equation on Unstructured Grids

Artur Guilherme Rodrigues de Vasconcelos
artur.vasconcelos@tecnico.ulisboa.pt

Instituto Superior Técnico, Universidade de Lisboa, Portugal

June 2017

Abstract

A very high-order finite volume method is proposed for the solution of the Poisson equation on unstructured grids based on the weighted least-squares method. The new method consists in a face centred reconstruction up to eight order of accuracy for the computation of the diffusive fluxes at the faces of the control volume. It uses a new stencil extension algorithm in order to maintain the local high order near the boundaries of the computational domain. To optimize the weight function a parametric study is performed based on convergence order and error magnitude of the schemes. From this study a new proposed weight function is defined for this type of reconstruction schemes. The results shown that the proposed method achieves the theoretical convergence order for Cartesian, triangular, polyhedral and hybrid grids, validating the proposed methodology. The memory requirements and solver-run time (SRT) indicates that the eight-order scheme is advantageous over the other lower order schemes, additionally it is shown that the polyhedral grid is superior to the Cartesian and triangular ones for these two efficiency criteria.

Keywords: Eight-order diffusive scheme, Finite volume method, Weight least-squares, unstructured grids, Weight function optimization, Poisson equation.

1. Introduction

The numerical solution of transport phenomena in complex physical geometrical configurations is a subject of continuous development regarding accuracy, robustness and efficiency. The geometrical complexity can be handled with different grid topologies such as polyhedral cells and their issues of robustness and efficiency are relevant for industrial applications. Particularly for aerospace, see e.g. Lê et al., [1], and Drikakis et al., [2], where high-order accurate methods for unstructured mesh finite volume (FV) computations have historically been focused on hyperbolic equations and in particular on advective fluxes.

Higher order (higher than second order) computation and particularly very high-order (higher than fourth order) is a demanding issue, motivated by a potential cost reduction for complex CFD computations. High-order methods have the potential to achieve an accurate solution with a coarse grid and a lower computational cost than a fine grid with a second order method, see e.g. Zing et al., [3], for structured grids and Lipnikov and Manzini, [4], for unstructured grids.

Barth and Frederickson, [5], were the pioneers on the development of a high-order Finite Volume Methods (FVM) for unstructured grids using a quadratic polynomial that results in a third-order scheme, which was applied for the resolution of the Euler equation. In last decades high-order methods have become very popular. This is highlighted in the polynomial reconstruction technique applied to FVM is highlight by Ollivier-Gooch et al., [6], Cueto-Felgueroso et al., [7], Nogueira et al., [8], with results have been reported up to sixth order by Clain et al., [9].

In the last years the resolution of parabolic and elliptic problems in unstructured grids has made significant progress, namely with the introduction of very high order methods, see e.g. Boularas et al., [9], Bertolazzi et al., [10], Droniou, [11]. Poisson problems, see Batty, [12], heat transfer problems, see e.g. Chantasiriwan, [13], diffusion equations with discontinuous coefficients, see e.g. Clain et al., [14].

Other applications includes the incompressible Navier-Stokes equations, namely for the projection methods, that requires the computation of face gra-

dients (diffusive terms) for the velocity field updates, presented in works of Nogueira et al., [8], and Guermond et al., [15].

These are some examples that use elliptic operators and they are the main reasons for the development of the very high order schemes in the Finite Volume (FV) framework.

2. Numerical Method

This section describes the FVM and the proposed weighted least-squares (WLS) scheme for diffusive term discretization of a transport equation. Details are provided on the stencil selection and how the global coefficient matrix is constructed according to the boundary condition.

2.1. Poisson Equation based on Finite Volume Method

The Poisson equation in the conservative form is given by:

$$\nabla \cdot \nabla \phi = \varphi_\phi, \tag{1}$$

where ϕ is the transported variable and φ_ϕ is the source term.

The Finite Volume (FV) discretization is based on the integral form of the conservative law (1) over a Control Volume (CV), resulting in the following expression

$$\int_{CV} \nabla \cdot \nabla \phi dV = \int_{CV} \varphi_\phi dV. \tag{2}$$

Applying the Gauss Divergence Theorem, the expression (2) can be written as

$$\int_{CS} \nabla \phi \cdot d\mathbf{S} = \int_{CV} \varphi_\phi dV, \tag{3}$$

where $d\mathbf{S}$ takes into account the unitary outward normal vector and surface area of the cell's faces.

Figure 1 shows the division of a typical continuous domain in non-overlapping volumes (cells). Several grids with triangular, quadrilateral and polyhedral cells with the information of the transported variable, ϕ, associated to each cell centroid was used.

Discretization of equation (1) with a FVM cell centered approach requires the calculation of the face gradient, $\nabla \phi_f$,

$$\sum_{f \in \mathcal{F}(P)} \sum_{g \in \mathcal{G}(f)} \nabla \phi_g w_G \cdot \mathbf{S_f} = \int_{CV} \varphi_\phi dV, \tag{4}$$

where $\mathcal{F}(P)$ is the set of faces of cell P, $\mathcal{G}(f)$ is the set of Gauss points of the face f, $\mathbf{S_f}$ is the face normal vector, w_G is the weight of Gauss-Legendre Quadrature.

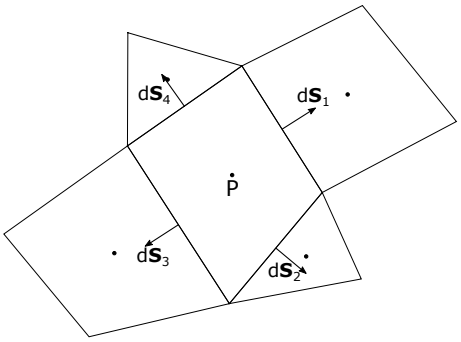

Figure 1: Cell-centered FV discretization over the CV P ($\bullet$ - *Cell Center*).

2.2. Least Squares Approach

2.2.1 Polynomial Reconstruction

To obtain the solution and its gradients at the integration points a reconstruction of the unknown primitive variable is performed to form a polynomial expansion about the control volumes face to the desired accuracy.

The polynomial reconstruction is performed taking into account the order of the numerical scheme and this is achieved by an expansion of a p^{th} complete polynomial, centered on the face where the reconstruction is made,

$$\phi_f^R(\mathbf{x}) = \mathbf{d}_f(\mathbf{x})\, \mathbf{c}_f. \tag{5}$$

The subscript f refers that the reconstruction is made at the face f centroid and $\mathbf{d}_f(\mathbf{x}) = \left[1, (x - x_f), (y - y_f), (x - x_f)^2, (y - y_f)^2, \cdots\right]$, and $\mathbf{x}_f = (x_f, y_f)$ is the face centroid coordinates, $\mathbf{x} = (x, y)$ is the coordinates of a point used for the reconstruction and $\mathbf{c}_f = [C_1, C_2, C_3, C_4, C_5, C_6, \cdots]^T$ are the reconstruction constants. The above expressions are valid for a p^{th} order complete polynomial and a polynomial reconstruction will be made for every face of the domain and will be called of Face Least Squares (FLS) approach. The number of terms of the expansion is given by $n_{coefs} = (p+1)(p+2)/2$,[17].

The order of accuracy of the numerical scheme is $p+1$ and consequently the linear reconstruction will be 2^{nd} order accurate, the cubic reconstruction will be 4^{th} order accurate, the 5^{th} polynomial will have 6^{th} order accurate and finally the 7^{th} polynomial will be 8^{th} order accurate. The numerical schemes will be called of $FLS(p+1)$ according to the order of the implemented method.

2.2.2 General Approach

Equation (5) results in a system of linear equations $\mathbf{D}_f \mathbf{c}_f = \boldsymbol{\phi}_s$, where $\mathbf{D}_f$ is a combination of $\mathbf{d}_f(\mathbf{x})$

for every point of the reconstruction resulting in a matrix with $(n_s \times n_{coefs})$ dimensions. The $\mathbf{c}_f$ is a column vector of n_{coefs} dimensions and $\boldsymbol{\phi}_s$ is a column vector with n_s dimensions, being n_s the size of the stencil (number of reconstruction points that will be explained in detail in next sections) and n_{coefs} is the number of constants of the p^{th} polynomial (unknowns). Since $n_s > n_{coefs}$, the WLS technique is needed to minimize the weighted residual, r, of the solution of the problem which is defined as:

$$\min\left(\mathbf{W}_{LS_f}\|\mathbf{r}\|^2\right) = \min\left(\mathbf{W}_{LS_f}\|\boldsymbol{\phi}_s - \mathbf{D}_f\,\mathbf{c}_f^T\|^2\right), \tag{6}$$

where $\mathbf{r} = \phi_s - \mathbf{D}_f\,\mathbf{c}_f^T$ and $\mathbf{W_{LS}}_f = \mathrm{diag}\left(w_{LS1}, \cdots, w_{LSn_s}\right)$ is the weight function of the LS problem that will be further analysed.

Differentiating (6) with respect to $\mathbf{c}_f$ and setting equal to zero yields:

$$\mathbf{D}_f^T\mathbf{W_{LS}}_f\mathbf{D}_f\mathbf{c}_f = \mathbf{D}_f^T\mathbf{W_{LS}}_f\boldsymbol{\phi}_s. \tag{7}$$

For clarity the matrix product will be defined as $\mathbf{D_w}_f = \mathbf{W}_{LS_f}\mathbf{D}_f$ and the unknown of the problem is $\mathbf{c}$. It is fundamental to ensure that the columns of $\mathbf{D}$ are linearly independent and the WLS solution can be expressed as:

$$\mathbf{c}_f = \mathbf{P}_f\boldsymbol{\phi}_s. \tag{8}$$

where the pseudo inverse matrix defined as $\mathbf{P}_f = \left(\mathbf{D_w}_f^T\mathbf{D}_f\right)^{-1}\mathbf{D_w}_f^T$. After the $\mathbf{P}$ matrix has been determined for every face of the domain it is possible to proceed with the construction of a linear system of equations of the Poisson problem because the constants of the reconstruction only depend of $\boldsymbol{\phi}_s$.

Equation (4) uses the fluxes through all the faces of the CV, given by the divergence of the reconstruction and obtained directly by taking the derivatives with respect to the coordinates directions and combining with equation (8) yields:

$$\nabla\phi_f^R(\mathbf{x}) = \left(\nabla\mathbf{d}_f(\mathbf{x})\right)\left(\mathbf{P}_f\boldsymbol{\phi}_s\right), \tag{9}$$

introducing the matrix $\mathbf{T}$ as:

$$\mathbf{T}_f(\mathbf{x}) = \left(\nabla\mathbf{d}_f(\mathbf{x})\right)\mathbf{P}_f \tag{10}$$

with dimension $(2 \times n_s)$, equation (9) can be expressed as $\nabla\phi_f^R(\mathbf{x}) = \mathbf{T}_f(\mathbf{x})\,\boldsymbol{\phi}_s$.

Equation (4) is valid for a generic CV, and applying it over all CV's results in a linear system of equations with the form $\mathbf{A}\boldsymbol{\phi} = \mathbf{b}$, where $\mathbf{A}$ is the Global Matrix with $(n_{cells} \times n_{cells})$ dimensions and $\mathbf{b}$ is a column vector with dimension n_{cells}, being n_{cells} the number of cells that the domain is divided.

Every line of $\mathbf{A}$ corresponds to a cell of the domain and each column corresponds to the contribution of a cell to the neighbouring ones for the calculation of the values of ϕ. The integration of the fluxes through the faces of the CV in equation (4) requires to use a Gauss Legendre Quadrature at least with the order of reconstruction, p, to maintain the reconstruction order of accuracy [18]. Consequently the left side of expression for the Poisson equation is given by:

$$\sum_{f\in\mathcal{F}(P)}\left(\sum_{g\in\mathcal{G}(f)}\mathbf{S}_f\cdot\left(\mathbf{T}_f(\mathbf{x}_g)\,\boldsymbol{\phi}_s w_{Gg}\right)\right), \tag{11}$$

where w_G is the weight of Gauss-Legendre Quadrature and $\mathbf{x}_g$ are the coordinates of the Gauss-Legendre Point of the face f. From the above expression the information for the construction of the global matrix is available, and each entry of the matrix $\mathbf{A}$ can be written in the following form:

$$A_{ij} = \sum_{f\in\mathcal{F}(i)}\left(\sum_{g\in\mathcal{G}(f)}\left(\mathbf{S}_f\cdot\mathbf{t}_{\mathbf{f}j}(\mathbf{x}_g)\right)w_{Gg}\right), \tag{12}$$

where i is the CV where the discretized equation is applied, j is the neighbour cell that is used for the face reconstruction f of CV and the column vector $\mathbf{t}_{\mathbf{f}j}$ is the column relative to the neighbour cell j of the face matrix $\mathbf{T}_f$ presented in expression (10). The determination right side of equation (2) will be further explained.

2.2.3 Interior Faces

A Stencil is the set of points used for the polynomial reconstruction and its choice is very important to the problem. The interior faces are free from the influence of the boundaries are described separately form the faces influenced by the domain boundaries.

The polynomial reconstruction is face centered and every face has a stencil associated to it, represented by $\mathcal{N}(f)$. The stencil should be as compact as possible and should have enough points in each direction to maintain the required order. In addition the stencil size, n_s takes into account the number of terms of the polynomial reconstruction, n_{coefs}. If $n_{coefs} > n_s$ the matrix $\mathbf{P}$ will be singular and the WLS problem will be ill conditioned and will not have an accurate solution [19]. Consequently $n_{coefs} < n_s$ is a necessary condition to have a overdetermined WLS problem [6, 19].

To have the most compact stencil possible the faces of the closest cells are selected. These cells are classified as first vertex neighbours of face f, i.e. the cells that have at least one common vertex with that face. The second order vertex neighbours, of a cell or a face, are the cells that share at least

one vertex with a cell that is a first order vertex neighbours, and so on for the other orders of vertex neighbours.

Figure 2 shows an example of the vertex neighbours that are used in the reconstructions of a face for an irregular polyhedral grid.

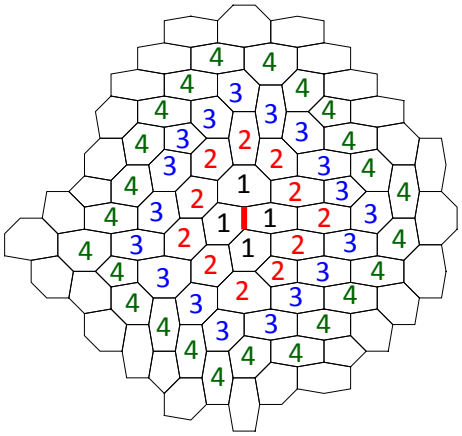

Figure 2: Example of the different orders of vertex neighbours of a face, marked in red, where the numbers inside of each cell represents the vertex neighbouring order of that cell with the face.

Tests performed to verify if the p^{th} polynomial reconstruction actually rebuilds a p^{th} complete polynomial have shown that in order to reconstruct the high order terms, it is necessary to have in each axis direction at least $p+1$ cells. For the faces far enough from the boundaries this requirement was always achieved with the proposed methodology.

2.2.4 Boundary Treatment

For a Dirichlet boundary the solution value is known and the face is added to the reconstruction stencil. As a consequence these stencils will included both cells and boundary faces, and this also applies for interior cells with boundary cells in the stencil. In addition, it is necessary to take into account the faces where the regression is being applied near the boundary (or on a boundary face) and do not satisfy the requirements mentioned previously ($n_s < n_{coefs}$, $n_x^s < p+1$ or $n_y^s < p+1$) where n_x^s and n_y^s are the number of points of the stencil in each axis direction, XX and YY respectively, with the superscript s denoting that the value refers to the stencil. For these situations it is necessary to perform a stencil extension to accomplish the referred requirements.

Once the initial stencil is constructed the following expression allows to know its size:

$$n_x^s = \frac{L_x^s}{h_{ref}^s} + 1.6, \tag{13}$$

where $L_x^s = x_{\max}^s - x_{\min}^s$ is the length in XX direction of the stencil, 1.6 is a factor that takes into account the fact that the cell and face centroids are used to calculate the stencil's length. The mean reference length of the stencil, L_{ref}^s, is given by:

$$h_{ref}^s = \frac{1}{n_{cells}^s} \sum_{i \in \mathcal{N}_c(f)} h_{ref}^i, \tag{14}$$

where n_{cells}^s is the number of cells in the stencil, $\mathcal{N}_c(f)$ is the set of cells of the stencil corresponding to face f and h_{ref}^i is the reference length of cell i. The calculation in other direction is performed similarly. When n_x^s, n_y^s or both is lower than $p+1$, the stencil will be extended in the respective direction. This operation is done for any face and repeated after an extension in order to verify if it was sufficient.

Figure 3 shows an example of a stencil extension for a cubic polynomial reconstruction at the marked boundary face, performed on a elliptic hybrid grid with Dirichlet boundary conditions. The initial stencil includes the first and second order vertex neighbours, numbered with the black color, and the boundary faces are marked with the blue color. In the YY direction the current stencil is long enough and will not grow in that direction, but in the XX direction it is necessary to perform a stencil expansion. To avoid cells in the YY direction a lower and upper YY bounds of the stencil is computed defined by $y_{\min}^s$ and $y_{\max}^s$, respectively, and represented by the dotted lines in the figure 3. Finally, the new cells added to the stencil after the extension are the third order vertex neighbours represented in figure 3 with the green color and numbered by 3.

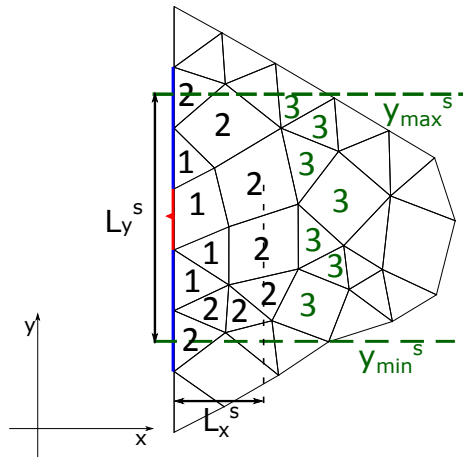

Figure 3: Example of a stencil extension in an elliptic hybrid grid for a cubic polynomial reconstruction for the face represented with the red color and the ◀ mark, the blue ones are the other boundary faces included in the regression.

2.3. Source Term

A high order Gauss Quadrature (GQ) for the integral of the source term of the Poisson equation, $\varphi_{\phi P}$ is also required. For two dimensional space the GQ can be directly applied for quadrilateral and triangular forms and any cell can be divided into triangular sub-cell. This work is related with 2D unstructured grids, so it becomes necessary to divide the non triangular cells into triangular sub-cells.

Simplex coordinates, $(\zeta_1, \zeta_2, \zeta_3, \cdots)$ are used to determine the Gauss integration points coordinates for each triangular element. A simplex region uses the number of points given the dimension space plus one, so for the 2D space will be necessary 3 points and the area coordinates are obtained according to Akin [20].

The integration of a triangular element is obtained by

$$I_\Delta(f) = S_\Delta \sum_{i \in \mathcal{G}(\Delta)} w_{G_i} f(\zeta_1, \zeta_2, \zeta_3), \tag{15}$$

where ζ_i denote the triangular coordinates, symplex region, of the triangular element, the respective area is computed by $S_\Delta = ((\mathbf{x}_1 - \mathbf{x}_3) \times (\mathbf{x}_2 - \mathbf{x}_3))/2$ and $\mathcal{G}(\Delta)$ is the set of Gauss points of the triangle Δ. The final expression for the integration of the source term is given by

$$\int_{CV} \varphi_\phi dV = \sum_{i \in \mathcal{T}(P)} \left(S_{\Delta_i} \sum_{j \in \mathcal{G}_i(\Delta_i)} w_{G_j} \varphi_\phi(\mathbf{x}_j) \right), \tag{16}$$

where $\mathcal{T}(P)$ is the set of triangular elements that the cell P was divided. The Gauss points coordinates of each triangular element are expressed as

$$\mathbf{x}_j = \boldsymbol{\zeta} \mathbf{x}_v, \tag{17}$$

where the $\mathbf{x}_v$ is the vertex coordinates of the triangular element.

3. Selection of the Weight Function

In this section a numerical test is presented to investigate the WLS weight function applied to two different grid types. The weight function and shape factor depends the level of accuracy according to Clain et al., [21].

In the present work several shape factors are compared for the WLS problem, which function is given by:

$$w_{LS_1}(\mathbf{x}_P) = \frac{1}{(d_{fP})^k}, \tag{18}$$

where $d_{fP} = \sqrt{(x_P - x_f)^2 + (y_P - y_f)^2}$ is the distance between the face f and the cell centroid P and k is the shape factor, which typically is equal to 2. This function was based on Ollivier et al., [6].

It was considered an analytical solution of Poisson equation given by:

$$\phi(x, y) = \exp\left(-\frac{(x - 0.5)^2 + (y - 0.5)^2}{0.0175} \right), \tag{19}$$

and the source term φ_ϕ evaluated according.

This work uses the error norm-1, $\|e\|_1$ and the norm-∞, $\|e\|_\infty$.

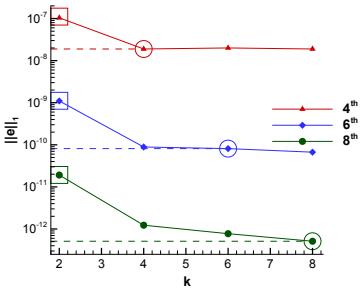

(a) Cartesian Grid with 25600 cells.

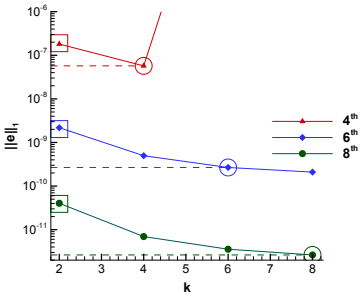

(b) Hybrid Grid with 47534 cells.

Figure 4: The $\|e\|_1$ for all high-order schemes, where the ◯ is the proposed shape factor for each diffusive scheme and the □ is the shape factor used by most authors.

The selection of the best k shape factor for the WLS formula was based on the accuracy analysis performed for each scheme, namely on the level of the numerical error. The selected weight function is very popular for WLS with $k = 2$, whatever of the order of convergence, see e.g. Gooch et al., [6, 22].

Figure 4 shows the accuracy of the schemes for a Cartesian grid and a hybrid grid for several shape factors. There is a significant difference between $k = 2$ and the others shape factors. From figure 4(a) the best shape factor for the Cartesian grid is $k = 8$, however for the $FLS4$ scheme the best result appears with $k = 4$ for the Hybrid grid, see figure 4(b). Consequently one may conclude that there is a relation between the convergence order of the scheme and the shape factor that will be considered to be equal to the order of convergence of scheme, $k = q$, where $q = p + 1$ is the theoretical order of convergence of the scheme.

Figure 4 compares the error $\|e\|_1$ for $k = 2$ and $k = q$. When k takes into account the order of the scheme, the solution accuracy is improved especially for the $FLS8$. Generally the accuracy increases for a k value equal to the order of the scheme. The error could be reduced substantially from 3 to 37 times the error obtained with $k = 2$, depending on the scheme and grid. The dotted lines in figure 4 shows that difference between k's. Similar conclusions presented in figure can be derived from the error $\|e\|_\infty$. From now on the weight function will be defined by:

$$w_{LS}\left(\mathbf{x}_P\right) = \frac{1}{\left(d_{fP}\right)^q}. \tag{20}$$

4. Numerical Schemes Verification

In this section several numerical tests under a different analytical solution are presented to investigate the influence of different grid types on the schemes' accuracy. Finally, this will be followed by an efficiency study where a comparison study between several grid types will be made, namely for the computational resources and time required.

The numerical verification was performed with the analytical solution of the Poisson equation with Dirichlet boundary conditions. The selected analytical solution is given by:

$$\phi\left(x, y\right) = \psi_1 - \psi_2 - \psi_3 + \psi_4, \tag{21}$$

where ψ_i is an auxiliary exponential function given by:

$$\psi_i = \exp\left(-120\left(\left(x - x_i\right)^2 + \left(y - y_i\right)^2\right)\right) \tag{22}$$

where the peaks have the following coordinates $(x_1, y_1) = \left(\frac{1}{3}, \frac{1}{3}\right)$, $(x_2, y_2) = \left(\frac{1}{3}, \frac{2}{3}\right)$, $(x_3, y_3) = \left(\frac{2}{3}, \frac{1}{3}\right)$ and $(x_4, y_4) = \left(\frac{2}{3}, \frac{2}{3}\right)$.

4.1. Influence of Grid Type

Numerical experiments were performed with four types of grids: Cartesian; hybrid; triangular and polyhedral.

Figure 5(a) shows the convergence curves of the schemes for the Cartesian grid. For the finest grid the error of the $FLS8$ scheme is close to the machine truncation error. The corresponding effective convergence order is equal to the theoretical value for the 1-norm. The error norms for $FLS8$ are almost nine orders of magnitude lower than the obtained with the second order scheme. Figure 5(b) shows similar values of the error norm and its effective convergence order for the finest triangular grids

The results obtained for irregular polyhedral grids (see figure 5(c)) also display the expected order of accuracy, it is also possible to verify that the higher order schemes are super convergent because the cells have more faces and the stencil is more compact when compared with the stencil obtained for other grid types. Note that once again the $FLS8$ reaches the machine truncation error. A regular polyhedral grid was also tested, the conclusions about the schemes are identical to the irregular polyhedral grid but the error obtained was one order of magnitude lower than the results presented for this grid.

Tests with an elliptic hybrid grid were also performed and presented in figure 5(d). The results show that the proposed method are robust with a convergence order close to the theoretical value.

Figure 6 shows a comparison of $\|e\|_1$ with the reference length using different grids for $FLS4$ and $FLS8$ schemes.

Figure 6(a) refers to the $FLS4$ scheme and the regular grids presents the better results for the same h_{ref}. For the smaller reference lengths it is verified that the triangular grid have a behaviour close to the Cartesian and regular polyhedral grids. The irregular polyhedral grid is the grid that presents the worse behaviour for $FLS4$ scheme if the hybrid grid is not considered for this comparison because it represents only a robustness test. However this behaviour changes for the $FLS8$ scheme, see figure 6(b).

The triangular grids have the worse behaviour and the regular polyhedral grids has the best behaviour and it is detached of the Cartesian one.

4.2. Efficiency Remarks

In this section the results of the efficiency study are presented firstly for the error level function of the non-zero entries of the global matrix, see Lipnikov and Manzini, [4], and secondly for the error level function of solver-run time, see Gooch, [23].

4.2.1 Non Zeros (NNZ)

A considerable reduction of the error norms was obtained for a very high order scheme, however the stencil is large and increase the computational cost and consequently the efficiency is a prime concern of the very high order numerical schemes. Denoting by N_z the number of non zero entries in the global matrix, Lipnikov and Manzini, [4], have reported that the error norm decay as $\mathcal{O}\left(h^q\right) \backsim \mathcal{O}\left(N_z^{q/D}\right)$, where D is the space dimension. For a two dimensional space, the error norm should decay $q/2$ with N_z, and the order of convergence can be calculated by:

$$\mathcal{O}_n^z = \frac{\log_{10}\|e\|_{n_1} - \log_{10}\|e\|_{n_2}}{\log_{10} N_{z_1} - \log_{10} N_{z_2}}, \tag{23}$$

where the superscript z means that the convergence order is related with N_z, which allows to estimate its size and consequently the amount of memory required for a determined error level.

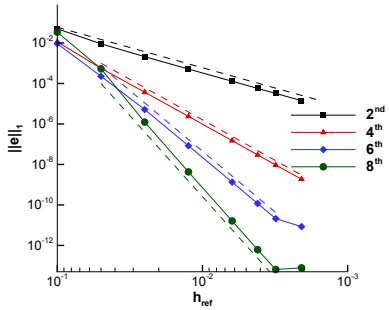

(a) $\|e\|_1$ for Cartesian grid.

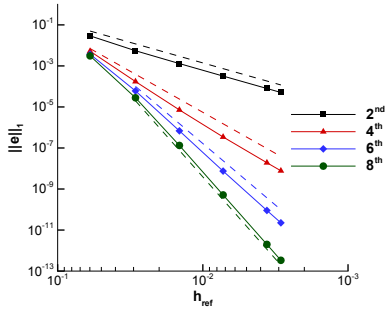

(b) $\|e\|_1$ for triangular grid.

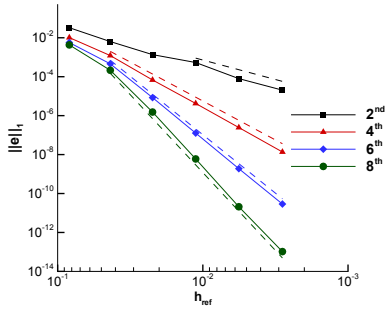

(c) $\|e\|_1$ for polyhedral grid.

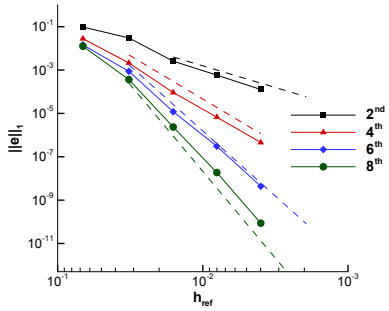

(d) $\|e\|_1$ for hybrid grid.

Figure 5: Convergence curves for all grid types for $\|e\|_1$ and all schemes, where the dotted line represents the theoretical slope of each scheme.

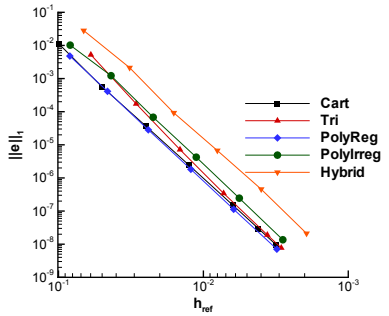

(a) $FLS4$.

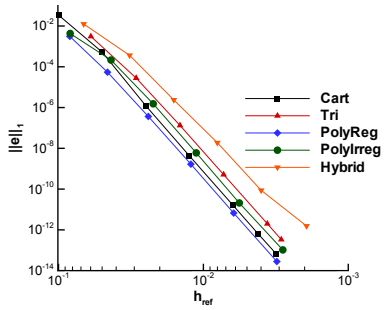

(b) $FLS8$.

Figure 6: Convergence curves of the error 1-norm with the h_{ref} for the different grids for $FLS4$ and $FLS8$.

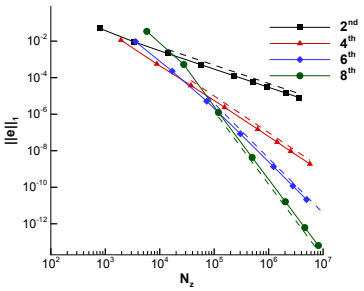

(a) Cartesian grid.

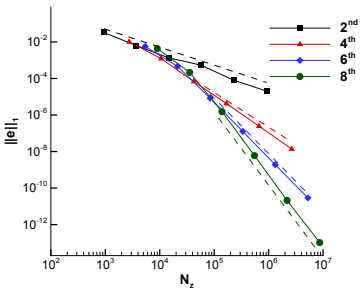

(b) Irregular polyhedral grid.

Figure 7: Convergence curves of error 1-norm functions of N_z with the Cartesian and polyhedral grids for different schemes, where the dotted line represents the theoretical slope of each scheme.

Figure 7(a) shows the results of $\|e\|_1$ vs N_z for all schemes with the respective theoretical convergence order being achieved for every scheme for the Cartesian grid. Figure 7(b) shows that the effective values of the convergence order for the polyhedral grids are in close agreement with the theory.

These results support that for the same error level a high order method can be more efficient than second order method because they would require less computational resources for the same accuracy level.

Table 1 lists the computational resources required to obtain a determined error level. The size of the global matrix is estimated multiplying N_z by 12 bytes, 8 bytes to allocate the value and 4 bytes to allocate the position in the matrix. The ratio is obtained by dividing the size of the global matrix of the selected scheme by the size of the global matrix for $FLS8$ scheme. The results show that the global matrix for $FLS8$ scheme occupies three to four orders of magnitude less computational storage than the $FLS2$, that means 7 times less than the $FLS4$ and almost half of the space is needed than the $FLS6$. These results allow to conclude that (with the same computational resources) the very high-order schemes will allow to obtain numerical solutions with higher accuracy than the second and fourth order methods.

4.2.2 Solver-Run Time (SRT)

Another form to analyse the method efficiency is through the computing time that the solver requires to achieved a converged solution, see e.g. [23]. For this study the BICGSTAB solver was used and figure 8(a) and 8(b) shows the results obtained for the Cartesian and polyhedral grids, respectively.

Figure 8 shows the errors level as function of the computing time required for convergence. Several grids were used and market from 1 to 8. For a certain level of error $FLS8$ scheme displays the fastest time for both grid types. The results shows that the error decays approximately with an $1/3$ power law of time, $\mathcal{O}\left(h^q\right) \sim \mathcal{O}\left(\left(t_{solver}\right)^{q/3}\right)$.

To obtain a certain level of error, $5.00\text{E}-09$, the SRT for $FLS8$ scheme is about half, 30 times and 10 millions times less than the SRT for $FLS6$, $FLS4$, $FLS2$ schemes for both Cartesian and polyhedral grids.

4.2.3 FLS8 Efficiency Variation with Grid Type

The accuracy and efficiency of $FLS8$ scheme is investigated for different grid types.

Figure 9(a) suggests that polyhedral grids optimize the computational resources. The triangular grid uses the largest stencil, one vertex of this grid type is connected with many cells increasing the

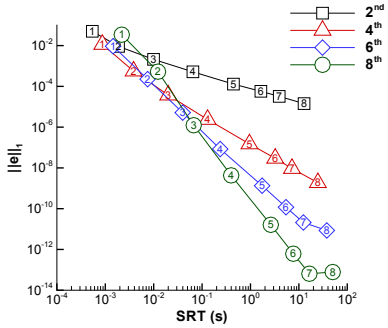

(a) Cartesian grid.

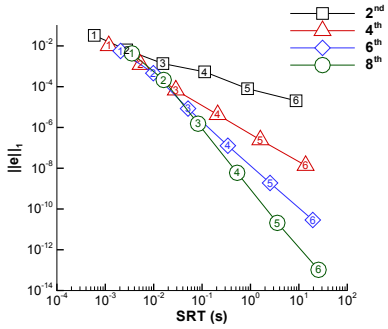

(b) Irregular polyhedral grid.

Figure 8: Mean error with SRT diagram for the proposed schemes with Cartesian and polyhedral grids.

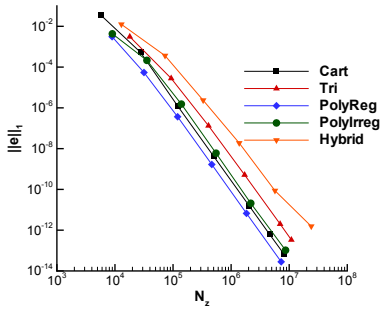

(a) NNZ.

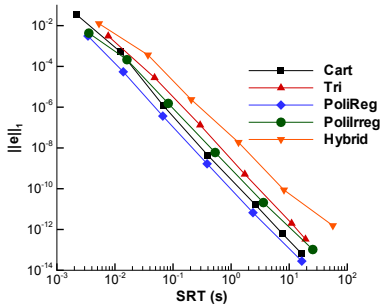

(b) SRT.

Figure 9: Convergence curves of the error 1-norm function of N_z (a) and SRT (b) for different grids types with the $FLS8$ scheme.

Table 1: Comparison of the computational resources required for all orders with a 1-norm level error of 4.30E-09 for Cartesian grid and 5.97E-09 for irregular polyhedral grid, where 1Gb = 1024Mb.

Scheme	Cartesian Grid $\|e\|_1 = 4.03E-09$				Irregular Polyhedral Grid $\|e\|_1 = 5.97E-09$			
	N_z	n_{cells}	size (**A**)	Ratio	N_z	n_{cells}	size (**A**)	Ratio
$FLS8$	4.98E+05	6.40E+03	5.70Mb	1.00	5.50E+05	8.32E+03	6.30Mb	1.00
$FLS6$	8.30E+05	1.76E+04	9.49Mb	1.66	9.08E+05	2.27E+04	10.40Mb	1.65
$FLS4$	3.77E+06	1.52E+05	43.17Mb	7.57	3.94E+06	1.95E+05	45.10Mb	7.16
$FLS2$	6.95E+09	7.74E+08	77.63Gb	13946.16	3.59E+09	5.13E+08	40.07Gb	6512.97

number of cells that defines the stencil, and consequently it requires more computational resources. Figure 9(b) refers to the SRT and suggests that regular polyhedral grids allows for accurate solutions obtained faster than with other grids. The triangular grid is the one with the worse behaviour, fact already expected because of the size of the matrix. Comparing with the triangular grid, one of the most used grid types nowadays, the polyhedral grids spends one third less time than the triangular one with the $FLS8$ scheme.

5. Conclusions

A new very high order scheme is proposed for the solution of the Poisson equation through polynomial reconstruction. A detailed description of the construction of the global matrix is included. Also a description was made of the new stencil selection technique, for both interior and boundary faces to reconstruct properly the high order terms. A parametric study was performed to select the weight function of the WLS reconstruction method, which to the Author knowledge it is new in the framework of these methods.

The presented method only require one reconstruction per face independently of the scheme's order. This is an advantage compared with other approaches that use a reconstruction per Gauss point. The main differences between this approach and the others high-order reconstruction approaches is the point value formulation and reconstructions centered at face centroid, which can be considered as an advantage because will not create flux discontinuities through the face. This new approach does not require an interpolation on the face that is used by the cell centered reconstructions.

The performed tests allowed to verify the effective convergence order of the new second, fourth, sixth and eighth order schemes flux least-squares reconstruction. In the framework of unstructured finite volume it is the first time that 8^{th} effective convergence order is reported for Poisson equation. The weight function optimization allows to decrease the error one or two orders of magnitude

Finally this study has the major conclusion that the polyhedral grid type is the one that required less computational resources for both required memory and SRT. These results are expected because the stencils for this grid type are smaller and more compact when compared with the other grids.

References

[1] T. H. Lê, J. M. Le Gouez, and E. Garnier. High accuracy flow simulations: Advances and challenges for future needs in aeronautics. *Computers & Fluids*, 43(1):90 – 97, 2011.

[2] Dimitris Drikakis, Dochan Kwak, and Cetin C. Kiris. Computational aerodynamics: Advances and challenges. *The Aeronautical Journal*, 120:13–36, 2016.

[3] D. W. Zingg, S. De Rango, M. Nemec, and T. H. Pulliam. Comparison of Several Spatial Discretizations for the Navier-Stokes Equations. *Journal of Computational Physics*, 160:683 – 704, 2000.

[4] Konstantin Lipnikov and G. Manzini. A high-order mimetic method on unstructured polyhedral meshes for the diffusion equation. *Journal of Computational Physics*, 272:360 – 385, 2014.

[5] Timothy Barth and Paul Frederickson. Higher order solution of the Euler equations on unstructured grids using quadratic reconstruction. In *28th Aerospace Sciences Meeting*, Aerospace Sciences Meetings. American Institute of Aeronautics and Astronautics, 1990.

[6] Carl Ollivier-Gooch and Michael Van Altena. A High-Order-Accurate Unstructured Mesh Finite-Volume Scheme for the Advection-Diffusion Equation. *Journal of Computational Physics*, 181:729 – 752, 2002.

[7] Luis Cueto-Felgueroso, Ignasi Colominas, J. Fe, Fermín Navarrina, and Manuel Casteleiro. High-order finite volume schemes on unstructured grids using moving least-squares reconstruction. Application to shallow water dynamics. *International Journal for Numerical Methods in Engineering*, 65:295 – 331, 2006.

[8] Luis Ramírez, Xesús Nogueira, Sofiane Khelladi, Jean-Camille Chassaing, and Ignasi Colominas. A new high-order finite volume method based on Moving Least Squares for the resolution of the incompressible Navier-Stokes equations on unstructured grids. *Computer Methods in Applied Mechanics & Engineering*, 278:883 – 901, 2014.

[9] A. Boularas, Stéphane Louis Clain, and F. Baudoin. A sixth-order finite volume method for diffusion problem with curved boundaries. *Applied Mathematical Modelling*, 42:401 – 422, 2017.

[10] E. Bertolazzi and G. Manzini. A unified treatment of boundary conditions in least-square based finite-volume methods. *Computers & Mathematics with Applications*, 49(11):1755 – 1765, 2005.

[11] Jerome Droniou. Finite volume schemes for diffusion equations: Introduction to and review of modern methods. *Mathematical Models and Methods in Applied Sciences*, 24(08):1575 – 1619, 2014.

[12] Christopher Batty. A cell-centred finite volume method for the Poisson problem on non-graded quadtrees with second order accurate gradients. *Journal of Computational Physics*, 331:49 – 72, 2017.

[13] S. Chantasiriwan. Methods of fundamental solutions for time-dependent heat conduction problems. *International Journal for Numerical Methods in Engineering*, 66(1):147 – 165, 2006.

[14] Ricardo Costa, Stéphane Clain, and Gaspar José Machado. *Finite Volume Scheme Based on Cell-Vertex Reconstructions for Anisotropic Diffusion Problems with Discontinuous Coefficients*, pages 87 – 102. Springer International Publishing, 2014.

[15] J. L. Guermond, P. Minev, and Jie Shen. An overview of projection methods for incompressible flows. *Computer Methods in Applied Mechanics & Engineering*, 195:6011 – 6045, 2006.

[16] H. K. Versteeg and W. Malalasekera. *An Introduction to Computational Fluid Dynamics*. Pearson Education Limited, 2nd edition, 2007.

[17] Jean-Camille Chassaing, Sofiane Khelladi, and Xesús Nogueira. Accuracy assessment of a high-order moving least squares finite volume method for compressible flows. *Computers & Fluids*, 71:41 – 53, 2013.

[18] Heitor Pina. *Métodos Númericos*. McGraw-Hill de Portugal, 1st edition, 1995.

[19] Luis Cueto-Felgueroso, Ignasi Colominas, Xesús Nogueira, Fermín Navarrina, and Manuel Casteleiro. Finite volume solvers and Moving Least-Squares approximations for the compressible Navier-Stokes equations on unstructured grids. *Computer Methods in Applied Mechanics & Engineering*, 196:4712 – 4736, 2007.

[20] J. E. Akin. *Finite Element Analysis with Error Estimators*. Elsevier, 1st edition, 2005.

[21] Stéphane Louis Clain, Gaspar J. Machado, J. M. Nóbrega, and Rui M. S. Pereira. A sixth-order finite volume method for multidomain convection-diffusion problem with discontinuous coefficients. *Computer Methods in Applied Mechanics & Engineering*, 267:43 – 64, 2013.

[22] Carl Ollivier-Gooch and Alireza Jalali. Higher-Order Finite Volume Solution Reconstruction on Highly Anisotropic Meshes. In *21st AIAA Computational Fluid Dynamics Conference*, Fluid Dynamics and Co-located Conferences. American Institute of Aeronautics and Astronautics, jun 2013.

[23] Amir Nejat and Carl Ollivier-Gooch. Effect of discretization order on preconditioning and convergence of a high-order unstructured Newton-GMRES solver for the Euler equations. *Journal of Computational Physics*, 227(4):2366 – 2386, 2008.